Journal of Cleaner Production 523 (2025) 146447

Contents lists available at ScienceDirect

Journal of Cleaner Production

journal homepage: www.elsevier.com/locate/jclepro

Performance and feasibility assessment of near-isothermal compressed air energy storage in aquifers

Zifeng Cheng [a], Daniel Dias-da-Costa [a], Yixiang Gan [a], Sheng Jiang [b,c], Luming Shen [a,*]

[a] School of Civil Engineering, The University of Sydney, NSW, 2006, Australia
[b] The National Key Laboratory of Water Disaster Prevention, Hohai University, Nanjing, 210098, China
[c] College of Water Conservancy and Hydropower Engineering, Hohai University, Nanjing, 210098, China

HIGHLIGHTS

- A framework for assessing I-CAES performance in deep aquifers is developed.
- The uncertainty within the geologic formation is included in the framework.
- High permeable deep aquifers have long-term large storage and efficiency.
- The best round-trip efficiency of 67 % is higher than 50 % of the existing D-CAES.
- Potential storage capacity in Gippsland Basin ranges from 0.88 to 1.48 TWh.

ARTICLE INFO

Keywords:
Compressed air energy storage
Aquifer
Round-trip efficiency
Near-isothermal process
Uncertainty analysis

ABSTRACT

Intermittent renewable energy sources such as wind and solar energy require large-scale energy storage systems to balance electricity production and demand. Near-isothermal compressed air energy storage (I-CAES) in aquifers can be a choice for large-scale energy storage with minimal greenhouse gas emissions. Since there is no existing commercial I-CAES in aquifers and field tests are limited, a numerical investigation is often the only pathway for assessing the technical feasibility and performance while addressing the challenges related to geological uncertainties. The novelty of this study lies in the development of a new framework for assessing the performance of I-CAES based on a coupled surface plant-wellbore-reservoir 3D model in conjunction with machine learning and uncertainty analysis. After conducting a geostatistical analysis with adopting the existing geological database, the feasibility of the I-CAES in aquifer is investigated using Gippsland Basin in Southeastern Australia as a case study. With the proposed framework, this study not only reveals the physical characteristics of a full process of the I-CAES but also assesses its feasibility under geological uncertainties. Results show that the round-trip efficiency of the I-CAES system can reach up to 67 % in highly permeable regions with no need of fuel combustion. It is also found that aquifer depth and permeability are the most significant geological factors affecting the output power and round-trip efficiency. The uncertainty analysis indicates that the daily storage potential in Gippsland Basin is found to range from 0.88 to 1.48 TWh with a corresponding probability of from 90 % to 10 %, which is equivalent to 116 %–181 % of the daily Australian electricity consumption in 2023. It is also demonstrated that there is no need of reheating expanded air with the proposed near-isothermal machinery, which is significantly advantageous than the conventional diabatic-CAES.

1. Introduction

The use of renewable energy sources such as wind and solar energy has been growing rapidly to reduce the reliance on traditional power sources such as fossil fuel. However, the balance between the intermittent generation of renewable energy and variation in electricity demand can pose significant challenges (Guo et al., 2021; Ziegler et al., 2019). According to the Australian Energy Market Operator (AEMO), the overall electricity demand in summer was 11 % higher than that in winter in 2024, and the peak demand during a day could be more than

* Corresponding author.
E-mail address: luming.shen@sydney.edu.au (L. Shen).

https://doi.org/10.1016/j.jclepro.2025.146447
Received 3 April 2025; Received in revised form 13 August 2025; Accepted 16 August 2025
Available online 22 August 2025

150 % of that in off-peak hours (AEMO, 2024). Therefore, grid-scale energy storage systems, which store surplus renewable energy for future demand could alleviate issues as well as improve the reliability and efficiency of energy supply. In terms of the form of energy storage, existing energy storage systems mainly include electrical energy storage (such as batteries and superconducting magnetic energy storage), thermal energy storage (such as phase-change material thermal storage) and mechanical energy storage (such as pumped-hydro energy storage). Among all types of existing energy storage systems, compressed air energy storage (CAES) is a promising technology considering its cost effectiveness, low green-house gas emission, as well as flexibility for longer duration and larger capacity. While the conventional battery storage systems provide short-duration storage with the discharge period up to 4 h (Denholm and Mai, 2019), a CAES system allows daily, weekly or even seasonal cycles to flexibly meet different grid-scale requirements (Bennett et al., 2022; Mouli-Castillo et al., 2019; Yang et al., 2020).

Generally, a CAES system stores surplus energy in the form of mechanical energy within the compressed air in underground formations. During high demand periods, the stored air is released and expanded through a turbine to generate power (Hounslow et al., 1998; Mahmoud et al., 2020; Tong et al., 2021). One of the main challenges for operating a CAES is to manage the extra high and low air temperatures during compression and expansion stages (Guo et al., 2021). Based on the technologies with regard to controlling the thermodynamic cycle of air, CAES systems can be classified into three categories: diabatic CAES (D-CAES), adiabatic CAES (A-CAES) and isothermal CAES (I-CAES) systems (King et al., 2021; Mahmoud et al., 2020; Tong et al., 2021). D-CAES is the traditional technology which requires fuel combustion to reheat the air during expansion (Guo et al., 2021). The main limitation for D-CAES is the significant amount of heat generated and lost during air compression (Elio et al., 2021). Furthermore, the extra combustion of fossil fuels not only results in a lower round-trip efficiency but also contradicts the goal of reducing green-house gas emissions. A-CAES and I-CAES can better mitigate the issues of the significant air temperature fluctuations during compression and expansion, as well as improving the round-trip efficiency with reduced thermal loss (Ghorbani et al., 2020; Yu et al., 2022; Zhou et al., 2020). A-CAES systems are coupled with storage systems for the extra thermal energy generated from air compression, which can then be used to reheat the air during the expansion phase (Zhou et al., 2019). While the efficiency can be significantly increased and the fuel combustion can be almost or fully avoided, the high temperature of the exhaust air is a potential drawback (Guo et al., 2021). Different from D-CAES and A-CAES, a near-isothermal process can be achieved using I-CAES systems, where the heat transfer enhancement such as liquid piston is used (Cheekatamarla et al., 2022; Li et al., 2023a; Qin and Loth, 2014).

Based on the type of storage reservoir, compressed air can be stored within salt caverns or porous media such as depleted gas reservoirs and aquifers (Guo et al., 2021; King et al., 2021). Salt caverns are safe and reliable for CAES while providing significant storage volumes. However, the natural salt caverns are not widely distributed and are usually far away from electricity grids. Porous reservoirs especially aquifers are much more widespread with larger capacity for potential air storage (Zhong et al., 2024). For example, highly pervious aquifers are widely distributed in Australia, *e.g.*, the Otway basin in South Australia and Gippsland basin in Victoria (O'Brien et al., 2008; Vidal-Gilbert et al., 2010).

Due to the mentioned advantages, CAES systems have been developed around the world. For example, there are two commercial CAES plants, Huntorf, Germany and McIntosh, USA and both are D-CAES with air stored in salt caverns. There are also CAES projects in China, such as the A-CAES in salt caverns in Jintan and Feicheng (Tong et al., 2021). However, CAES in aquifers are still limited, and there is no commercial CAES plants in aquifers with either adiabatic or isothermal cycles. The Pittsfield test performed in the US in 1981 is regarded as the only demonstration of the feasibility of CAES in aquifers (Allen et al., 1985). Moreover, a project was planned for developing a D-CAES in aquifer in Iowa, but ceased in 2013 due to geological and economic challenges (Schulte et al., 2012).

The performance of CAES in aquifers has been numerically investigated in recent years. Kushnir et al. (2010) proposed an approximate analytical solution for a representative case in which the water coning problem was identified as critical to control the air production. One advanced numerical study on CAES in aquifers was carried out by Oldenberg and Pan (Oldenburg and Pan, 2013a), who developed 2-D numerical models based on TOUGH2 to study the essence of CAES in porous media in terms of the capability of pore space, round-trip efficiency, effect of pressure and water movements. In addition, the effect of various cycle modes was numerically investigated, such as the comparison of daily, weekly and monthly cycles for CAES in aquifers (Allen et al., 1983; Yang et al., 2020), and the investigation of seasonal cycles for CAES in aquifers (Li et al., 2023b; Mouli-Castillo et al., 2019). Some research was extended to study the effect of different gas medias. For example, Oldenburg and Pan (2013b) studied the use of CO2 as cushion gas in CAES in aquifers, and Li et al. (2022) compared the performance of systems using pure CO2 and pure air. Due to the computational cost, most existing numerical studies focused on a single CAES site with one well or several wells, and the size of reservoir in these studies ranged from 3 km to 16 km (Li et al., 2022; Oldenburg and Pan, 2013b; Wang and Bauer, 2017). Aquifers usually extend to hundreds of kilometres requiring hundreds of or even thousands of wells. It is, therefore, important to estimate the overall storage potential of CAES to meet the significant electricity demand instead of focusing on smaller regions. Accordingly, there is a need to conduct a systematic assessment for the I-CAES in regional scale to quantify its performance and identify suitable areas. Also, a gap exists between the need for regional-scale assessment and relatively small scale of existing numerical studies. In addition, the complexity of subsurface conditions is always crucial for geological analysis (Fukai et al., 2020). Therefore, it is necessary to develop a systematic method for assessing regional-scale I-CAES with probability evaluation for geological uncertainties.

This research aims to develop an integrated framework to numerically investigate the performance of a proposed near-isothermal CAES system and assess its technical feasibility at regional scale with the consideration of geological uncertainties. As a result, the current research gap between the need for regional-scale assessment and the existing small scale numerical studies can be addressed. In this study, an integrated method is developed to evaluate the storage potential of I-CAES systems at a regional scale. The storage potential for I-CAES in Gippsland Basin in south-east Australia is used as a case study. The highly pervious Latrobe aquifer widely distributed within Gippsland Basin could provide enormous potential for large-scale air storage. The site was identified to have both impervious caprock and base rock to constrain the injected air. According to the Department of Climate Change, Energy, the Environment and Water (DCCEEW), a 25 GW offshore wind farm is under development (DCCEEW, 2024), which presents a unique opportunity to combine the proposed I-CAES with surplus wind energy. The performance of a single I-CAES site is first studied with an integrated framework, which consists of a reservoir model, a well model and a thermodynamic analysis for the surface plants. The obtained numerical results investigate the relationship between I-CAES performance (including output power and round-trip efficiency) and all parameters from underground reservoir, wells and surface plants. To investigate the influence of geological uncertainties on I-CAES performance, Monte Carlo (MC) analysis is deployed to consider the uncertainties of physical parameters in the underground reservoir. The MC analysis is combined with a machine learning (ML) model or a surrogate model trained with the numerical results. After obtaining the full spatial distribution of all parameters based on the existing geological dataset in Gippsland Basin, the trained machine learning model is applied for uncertainty analysis using Monte Carlo

sampling of all parameters.

2. Methodology

The integrated framework proposed in this study combines numerical modelling, machine learning and uncertainty analysis to investigate the performance of I-CAES and its technical feasibility at regional scale. The open-source code Matlab Reservoir Simulation Toolbox (MRST) was used for reservoir modelling (Lie, 2019), while a Gaussian Process Regression model was used as the machine learning model. Firstly, a conceptual I-CAES with heat enhancement machinery is proposed. The Central Deep area within Gippsland Basin in southeastern Australia is taken as a case study. The entire daily cycle of each I-CAES grid is analysed by modelling reservoir, wells and surface plants. The machine learning, which is trained by the numerical results, is then used as a proxy model. Finally, an overall uncertainty analysis using Monte Carlo approach is used for estimating the overall storage potential of the study region. The detail of each step is explained in the remaining content in this section.

2.1. Conceptual model

The schematic illustration of the proposed conceptual I-CAES system is shown in Fig. 1, which is composed of three parts: 1) a pervious aquifer sealed with impermeable cap and bottom rocks; 2) a well for air injection and production; and 3) surface plants with heat transfer enhancement machinery to achieve near-isothermal compression and expansion. With the use of isothermal machinery, the temperature change during compression and expansion can be significantly reduced so there will be minimal need to include any combustor for reheating air during production. The proposed I-CAES also cooperates with wind energy, since the selected area is co-located with a potential 25 GW offshore wind farm which is expected to be finished in early 2030 (DCCEEW, 2024).

The workflow of this study is shown in Fig. 2. First, the Gippsland Basin located in southeastern Australia was selected as the study area with reference to all related geological information (namely, aquifer thickness, depth, permeability and porosity). To understand the physical mechanisms and critical parameters which dominate the performance of the I-CAES, we then used numerical and analytical models to analyse a single system with an injection/production well located at the centre of a 2 km × 2 km grid. A sensitivity study was also performed based upon 256 models, where representative values of all four geological parameters were chosen. Next, the results from parametric study from I-CAES modelling with varying parameters were used for training the ML model.

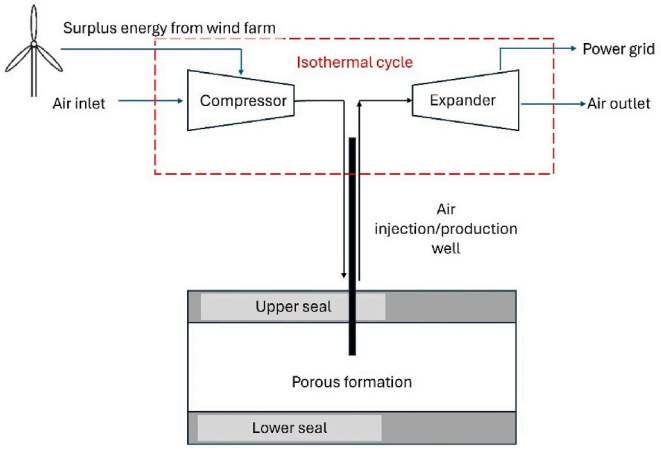

Fig. 1. Schematic illustration of a conceptual I-CAES system in an aquifer (note: the red box with dashed line indicates the isothermal cycle for air compression and expansion).

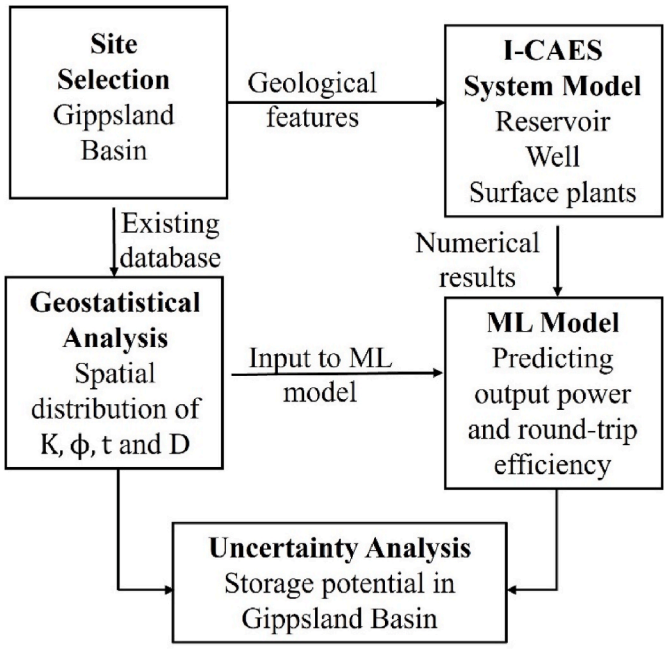

Fig. 2. Flowchart of the overall process to analyse the performance of proposed I-CAES and its application for utility-scale storage assessment.

This model was able to predict I-CAES performance for any value of geological parameters within the range, which was further used in the uncertainty analysis. Furthermore, geostatistical analysis using Kriging method (Hohn, 1999) was conducted based on the geological database of Gippsland basin to obtain the spatial distribution of four geological parameters. Finally, the trained ML model as a surrogate of the I-CAES modelling coupled with the geological data was used for estimating the storage potential of the whole region including the uncertainty analysis.

2.2. Site selection

The Gippsland Basin located in southeastern Australia is selected for this study. The highly permeable aquifer, named Latrobe aquifer, is widely distributed here with the total area of approximately 45,000 km^2 (Malek, 1998; O'Brien et al., 2008; Varma et al., 2010). The thickness of Latrobe aquifer ranges from 100 m up to 2500 m within the Central Deep area, which provides significant potential for large-scale CAES systems. In addition, the permeable Latrobe aquifers are beneath the impervious Lakes Entrance aquitard (as shown in Fig. 3) and above the Strzelecki

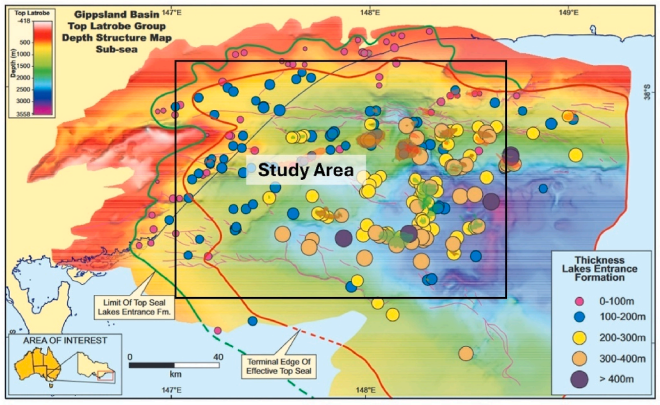

Fig. 3. Location map of Gippsland basin with Lakes Entrance Formation (top seal rock) thickness and depth of top aquifer (O'Brien et al., 2008). The black box marks the region of interest investigated in this study.

aquitard in most areas, of which the structure can provide sufficient top and bottom constrains for air storage. This study focuses on the Central Deep area with a size of 200 km × 108 km, not only because the Latrobe aquifer within this area is thicker with higher storage potential, but also because there are existing gas/oil production wells which could be further used for CAES. Furthermore, from an economic point of view, this area is closer to the potential offshore wind farm (DCCEEW, 2024).

2.3. I-CAES system model

To quantitatively investigate the performance of an entire process of I-CAES in aquifer, a single I-CAES system is selected to perform the numerical simulations. The grid for a single system was sized as 2 km × 2 km, and the entire study area was divided into 5400 grids. The system size was determined with considering the amount of cushion gas, the maximum flow rate for the well and the maximum injection pressure. The analysis of the single complete I-CAES system is divided into three parts. First, a 3-D numerical model for the underground reservoir was built to simulate the pressure distribution and air plume evolution within the reservoir. Next, an analytical model was created for the injection/production well to address the pressure and temperature loss within the wells. Finally, a thermodynamic analysis for near-isothermal process within surface plants was conducted to obtain input and output powers, and the overall round-trip efficiency was also calculated accordingly.

2.3.1. Reservoir model

MRST was used for the numerical simulations of reservoir in this study (Lie, 2019; Lie and Møyner, 2021). The Black-Oil module was adopted for analysing the system with up to three phases in a porous medium. The general form of mass conservation equation for an arbitrary domain Ω with boundary Ω , which is solved by MRST, can be written as (Lie, 2019):

$$\frac{\partial}{\partial t}\int_{\Omega}\phi\rho_{\alpha}S_{\alpha}\,d\Omega+\int_{\partial\Omega}\rho_{\alpha}\vec{v_{\alpha}}\cdot\vec{n}\,ds=\int_{\Omega}q_{\alpha}\,d\Omega, \tag{1}$$

where ϕ is the rock porosity, ρ_α is the density of the fluid component α, S_α is the saturation, $\vec{v_\alpha}$ is the Darcy velocity, s is the surface on domain boundary $\partial\Omega$, q is sinks and sources and $\vec{n}$ denotes the normal vector on surface $\partial\Omega$.

The Darcy's law for multiphase flow using the concept of relative permeability is written as (Lie, 2019; Muskat and Meres, 1936):

$$\boldsymbol{v}_{\alpha}=-\frac{\boldsymbol{K}k_{r\alpha}}{\mu_{\alpha}}(\nabla p_{\alpha}-\rho_{\alpha}\boldsymbol{g}), \tag{2}$$

where $\boldsymbol{v}_\alpha$ is a vector of Darcy velocity of phase α, $\boldsymbol{K}$ is a tensor of absolute permeability, $k_{r\alpha}$ is the relative permeability of phase α, μ_α is the dynamic viscosity, p_α is the pressure, ρ_α is the density and $\boldsymbol{g}$ is the gravitational acceleration vector.

The Brook-Corey equation was used to describe the relationship between capillary pressure and saturation in the porous media. The capillary pressure and saturation relationship is mathematically described by (Corey, 1954; Lie, 2019):

The Brook-Corey equation was used to describe the relationship between capillary pressure and saturation in the porous media. The capillary pressure and saturation relationship is mathematically described by:

$$S_e=\left(\frac{P_c}{P_e}\right)^{-\lambda}, \tag{3}$$

where S_e is the effective saturation, P_c is capillary pressure, P_e is entry pressure at which gas starts to enter the largest pores, and λ is the pore size distribution index. The initial setting values of parameters for reservoir model are shown in Table 1.

Table 1
Parameters of the aquifer and wells for the reservoir model.

Parameters	Values
Grain density	2400 kg/m^3
Relative permeability function	Brook-Corey model (Muskat and Meres, 1936)
Capillary pressure function	Brook-Corey model (Muskat and Meres, 1936)
Fitting parameter λ	0.5
Saturated liquid saturation	1.0
Residual liquid saturation	0.1
Residual gas saturation	0.05
Skin factor	1.0
Well diameter	0.3 m
Injection and production length of well bottom	3 m

The numerical model of the single I-CAES system with one injection/production well at the centre, a representative flat reservoir grid size of 2 km × 2 km × 220 m was taken. As shown in Fig. 4 (a), the thicknesses of the caprock, the aquifer and the base layer are 100 m, 100 m, and 20 m respectively, while the isotropic permeabilities for these layers are 0.1 mD, 1000 mD and 0.1 mD, respectively. The injection/production well located at the centre of the reservoir grid with the well bottom located at the interface between the caprock and the top aquifer. Horizontally, the reservoir grid was discretised into 39 × 39 cells with refined meshes (0.5 m × 0.5m) around the well and coarse mesh (100 m × 100 m) near the boundaries, as shown in Fig. 4(b). The model was vertically divided into 20 layers with the finest thickness of 5 m around the well bottom. The total number of elements was 26,163. A mesh convergence study was conducted, showing that the adopted mesh size could ensure the convergence and stability of the simulation. Using a uniform small horizontal size of 1 m for all elements and smaller refined vertical size around the well bottom would not significantly change the results.

It is assumed that the reservoir is initially saturated with water. Accordingly, the initial pressure distribution within the reservoir is equal to the hydrostatic pressure with 100 % water saturation. The top and bottom boundaries are set as closed boundaries with no flux. Since the model represents a single site surrounded by neighbouring sites (except for those grids located at the edges of the 200 km × 108 km region), it is acceptable that the lateral boundaries are defined as no-flux as the flows at the two sides of each lateral boundary compensate each other.

The two-phase flow (air-water) was simulated by considering air as a compressible phase and water as incompressible phase. The temperature of ambient air is 20 °C and the geothermal gradient is set as 34 °C/km (Malek, 1998). The process was assumed as isothermal given that the temperature of the compressed air is very close to the reservoir temperature by using the near-isothermal surface plants. Results from the literature also show that the temperature of air from the wellbore only affects the temperature of an extremely small range around the well bottom with the remaining domain of the reservoir nearly unaffected. For example, with a temperature difference of 20 °C between well and reservoir, the range of temperature influence is only about 10 m–20 m around the well (Li et al., 2020).

2.3.2. Well model

The well model is also an essential part of the modelling of a CAES as both the pressure and the heat losses within the injection/production wells can result in lower efficiencies. The analytical solution from Hagoort was applied for determining the well effects (Hagoort, 2005). The solution is based on the extended Bernoulli equation and the energy balance equation. The extended Bernoulli equation for a length element dy is shown below (Hagoort, 2005):

$$\mathrm{d}p+\frac{Mg\cos\alpha}{zR}\frac{p}{T}\,dy+\frac{2zfw^2R}{A^2\mathrm{d}_hM}\frac{T}{p}dy=0, \tag{4}$$

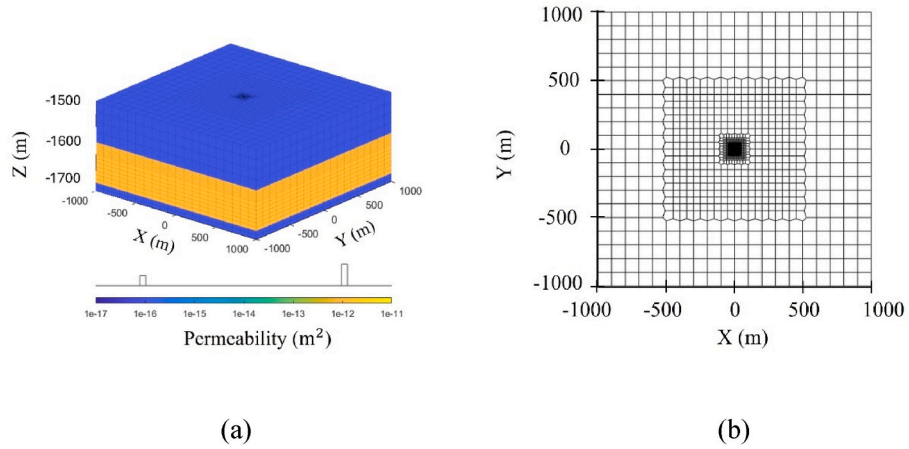

Fig. 4. Numerical setup for a single I-CAES system in aquifer: (a) 3-D illustration of system size with vertical distribution of permeability; and (b) domain discretisation.

where p is the pressure, M is the molecular mass, g is the gravitational acceleration, α is the inclination of the well, z is the compressibility factor, R is the gas constant, T is the absolute temperature, y is the direction along the well, f is the Fanning friction factor which is an empirical function with regard to Reynolds number and wall roughness, w is the mass flow rate, A is the cross-sectional area of well and d_h is the well diameter. The energy balance equation is written as follows (Hagoort, 2005):

$$\mathrm{d}H + Mg\cos\alpha\,\mathrm{d}y = \mathrm{d}Q, \tag{5}$$

where dH is the enthalpy change and $Mg\cos\alpha\,dy$ is the potential energy change, while dQ is the heat being added to the gas flow.

2.3.3. Near-isothermal process for surface plants

After obtaining the well bottom pressures from the reservoir model and the well head pressures from the well model, the output power and the round-trip efficiency for an entire cycle was determined by the analysis of surface plants (a compressor and an expander). The analysis of near-isothermal process was based on the equations for polytropic process. The polytropic process is widely used for describing non-ideal gas behaviours between isothermal and adiabatic conditions. The general relation is written as:

$$pV^k = C, \tag{6}$$

where p is the pressure, V is the volume, k is the polytropic index and C is constant.

The output work from the expander is calculated as (Dib et al., 2021):

$$W = \frac{p_2V_2 - p_1V_1}{1-k}, \tag{7}$$

where subscripts 1 and 2 denote the conditions before and after the expansion. That is, p_2 and V_2 are the pressure and volume of air at the outlet of the expander, while p_1 and V_1 are of the pressure and volume of air at the inlet of the expander. The polytropic index k, also known as the specific heat capacity ratio, dominates the type of thermodynamic processes. It is 1.4 for adiabatic process and 1.0 for pure isothermal process (Cengel et al., 2020). From the literature, the polytropic index for existing near-isothermal machinery ranges from 1.04 to 1.21 (Bennett et al., 2022; Patil et al., 2020; Zhang et al., 2018). Since the polytropic index of 1.04 can be achieved within the existing heat transfer enhancements this value was assumed in this study. The output power can be correspondingly calculated using the volumetric flow rate to replace the air volume in the equation. Then the outlet temperature is calculated using

$$T_2 = \left(\frac{p_2}{p_1}\right)^{\frac{1-k}{k}} T_1, \tag{8}$$

where T_2 and T_1 are the outlet and inlet air temperatures for either compressor or expander, respectively. Knowing the air temperature and pressure at the inlet of the compressor, equations (4) and (5) can also be used for the compression stage to obtain the power and temperature at the outlet of the compressor after the compression. Accordingly, the polytropic index, pressures at the inlet and outlet of compressors and expanders, will influence the behaviour of surface plants. As shown in Eqs. (7) and (8), the polytropic index k is the major parameter influencing the process. A smaller k being close to 1 could increase the work generated, as well as decreasing the temperature difference of T_1 and T_2. The pressure difference between p_1 and p_2 also has impacts on the outlet temperature T_2. Then the round-trip efficiency (RTE) of an entire cycle can be calculated accordingly. The RTE is defined as the ratio of total produced energy at the outlet of the expander to the total injected energy at the inlet of the compressor, and is mathematically described as:

$$\eta_{RTE} = \frac{W_{prod}}{W_{inj}}\eta_{comp}\eta_{exp}, \tag{9}$$

where W_{prod} and W_{inj} are the output energy and input energy during production and injection phases, while η_{comp} and η_{exp} are the mechanical efficiencies of the compressor and the expander which are assumed to be both 85 % in this study.

2.4. Uncertainty analysis

The results from the I-CAES model were then used to investigate the overall performance of Gippsland Basin with uncertainty analysis. Predictive machine learning models trained by numerical results were applied for the uncertainty analysis. The full geological map of the entire studied area was obtained by geostatistical analysis, where limited information from gas/oil fields were used for estimating the geological properties of all 2 km × 2 km grids. Finally, Monte Carlo approach was applied for addressing geological uncertainties, and the overall storage potential with various probability was obtained.

2.4.1. Predictive machine-learning model

To reduce the computational cost, predictive machine learning (ML) models were trained and applied for predicting the relationships between the dependant variables (output power and round-trip efficiency) and predictors (permeability, porosity, aquifer depth and thickness, which are the key geological parameters identified above). The Gaussian

Process Regression (GPR) model was used, which is nonparametric and kernel-based probabilistic. The nonisotropic Matern 3/2 kernel function was adopted. The type of kernel function was tuned as main hyperparameter in this study, which was optimised by Bayesian optimization.

2.4.2. Geostatistical analysis: Kriging method

The main challenge for modelling reservoir is associated with the complexity of a geological formation and the limited information of data from core logging. There are 32 gas/oil fields within the Central Deep area of Gippsland Basin, where the geological data is known from the geologic samples. To obtain the full maps of all geological parameters, the Kriging method was used for the spatial interpolation. Kriging is a regression algorithm for spatial modelling and prediction of random processes/random fields based on covariance functions. The interpolation accuracy of the Kriging model was assessed by performing leave-one-out cross-validation (LOOCV), where all data points except one were iteratively trained until all points were validated. The mean absolute error (MAE) and the coefficient of determination (R^2) values were used to measure the predictive accuracy. The general form of the Kriging method is written as:

$$\widehat{Z}(s_0) = \sum_{i=1}^{N} \lambda_i Z(s_i), \tag{10}$$

where s is the coordinates representing a location in the spatial domain, $Z(s_i)$ is the value measured at the location i, λ_i is the weight of the measured value which depends on not only the spatial relationship between the measurement points but also the prediction point as well as the spatial relationship within a certain range (Ricciardi et al., 2005).

2.4.3. Monte Carlo analysis

With the Kriging method, the full map of all geological parameters can be generated with representative values at each single CAES site. To further address the uncertainty within the geologic formation, each geological parameter was then represented by a distribution. Here the distribution of parameters is based on the available characterisation of the Latrobe aquifer in the Gippsland Basin from Hurter et al. (2013), in which the authors used a normal distribution for porosity and depth, and a lognormal distribution for permeability and thickness. We performed 100 iterations for each CAES grid. The number of Monte Carlo iterations was determined by the standard deviation threshold. The simulation was determined to be converged when the standard deviation is less than 0.1 %. With the distribution of all four parameters defined, the predictive ML model was applied to perform the Monte Carlo analysis for output power and round-trip efficiency.

2.4.4. Section 2.5 cost estimates

Cost estimates of the proposed I-CAES system were calculated using the levelised cost of electricity (LCOE) (Matos et al., 2023), which is represented by

$$LCOE = \frac{\sum_{t=1}^{n} \frac{W_t + T_t + C_t + M_t}{(1+r)^t}}{\sum_{t=1}^{n} \frac{E_t}{(1+r)^t}}, \tag{11}$$

where subscript t is the year, W_t is the initial cost of well drilling, T_t and C_t are the capital cost of the turbine (expander) and the compressor, M_t is the operation and maintenance (O&M) cost, E_t is the generated electricity and r is the discount rate.

3. Modelling of a single I-CAES

In this section, the results from the modelling of a single I-CAES grid are included. The modelling consists of three components: a reservoir model, injection/production well model and surface plant model. With these three models, the temperature and pressure change within the entire daily cycle can be generated, as well as the overall round-trip efficiency indicating the performance of the proposed I-CAES. All relevant results are presented within the remaining contents of this section.

3.1. Pressure performance and gas saturation in aquifer

The base model was designed based on the geological dataset with adjusted flow rates. Permeability, porosity, aquifer depth and aquifer thickness were identified as the four crucial parameters in reservoir modelling. Based on the range of all four parameters as well as their distributions in Gippsland Basin, the permeability, porosity, aquifer depth and aquifer thickness for the base model were set as 1000 mD, 17 %, 1500 m and 100 m respectively. To be representative, the values of the former two parameters were taken as middle values within the range, while the latter two were chosen using the most distributed values within the region. The mass flow rate of air injection and production was 40 kg/s, which was determined with the consideration of the maximum injection pressure, stabilisation of production pressure and well capacity. From the literature, the cushion gas ranged from 10 to 100 times of the working cycle gas (Guo et al., 2021). Therefore, an initial air bubble with mass being 40 times of working gas was selected, which is sufficient for providing pressure support for minimising water coning while the maximum pressure in the reservoir is still under the limit state. Accordingly, the injection of cushion gas is at flow rate of 40 kg/s for 20 days, followed by 100 daily cycles with 12 h injection and 12 h production. It was observed that the injection and production behaviours tend to be stable after 100 cycles for all cases with their permeability no smaller than 1000 mD.

Fig. 5(a)–(c) show the development of air bubble after cushion gas injection and after 100 daily cycles. The cross section at middle (i.e. at Y = 0 m) is taken for all figures in Fig. 5. Initially, the air bubble forms a cone shape around the well bottom with horizontal extension of about 400 m at each side and maximum thickness of about 50 m. After 100 cycles, the air bubble tends to float up to the interface between top aquifer and cap rock. The corresponding profiles of pressure distribution are shown in Fig. 5(d)–(f). The region around the well bottom has a sharp pressure increase after cushion gas injection, and the size of horizontal extension of pressure increase area is similar to the air bubble. The pressure distribution smears after the operation of a few cycles, and the pressure around the well decreases to maintain the constant production.

To better monitor the pressure performance, the well bottom pressure during the cycle operations was extracted in Fig. 6. The injection pressure remained almost stable among all cycles, with a value close to 21.0 MPa. The production pressure dropped to 20.4 MPa after the first cycle. With the continuation of cycles, the production pressure initially decreased quickly and then gradually stabilised at around 18.2 MPa. The movement of air bubble results in the reduction of air around the well bottom, and the lack of air below the well bottom requires a larger pressure difference between reservoir and well bottom to extract the air.

3.2. Losses in injection/production wells

With the bottom hole pressures obtained from the reservoir model, the well head pressures as well as the temperature loss for both injection and production were calculated from the well model by considering friction losses, heat loss from well wall and gravity effects. The results of the sensitivity analysis for the well model are shown in Fig. 7, where the effects of flow rate, well diameter and length on well head pressures are shown under the bottom hole pressure of 18.2 MPa for the base model. A noticeable pressure drop was observed for the cases with well diameter of 0.15 m. The pressure drops also increased with the well length. With the range of the flow rates in this study, the well head pressures for the cases with diameters of 0.3 m and 0.45 m were found to be almost identical. Therefore, diameter of 0.3 m was selected, which also aligns

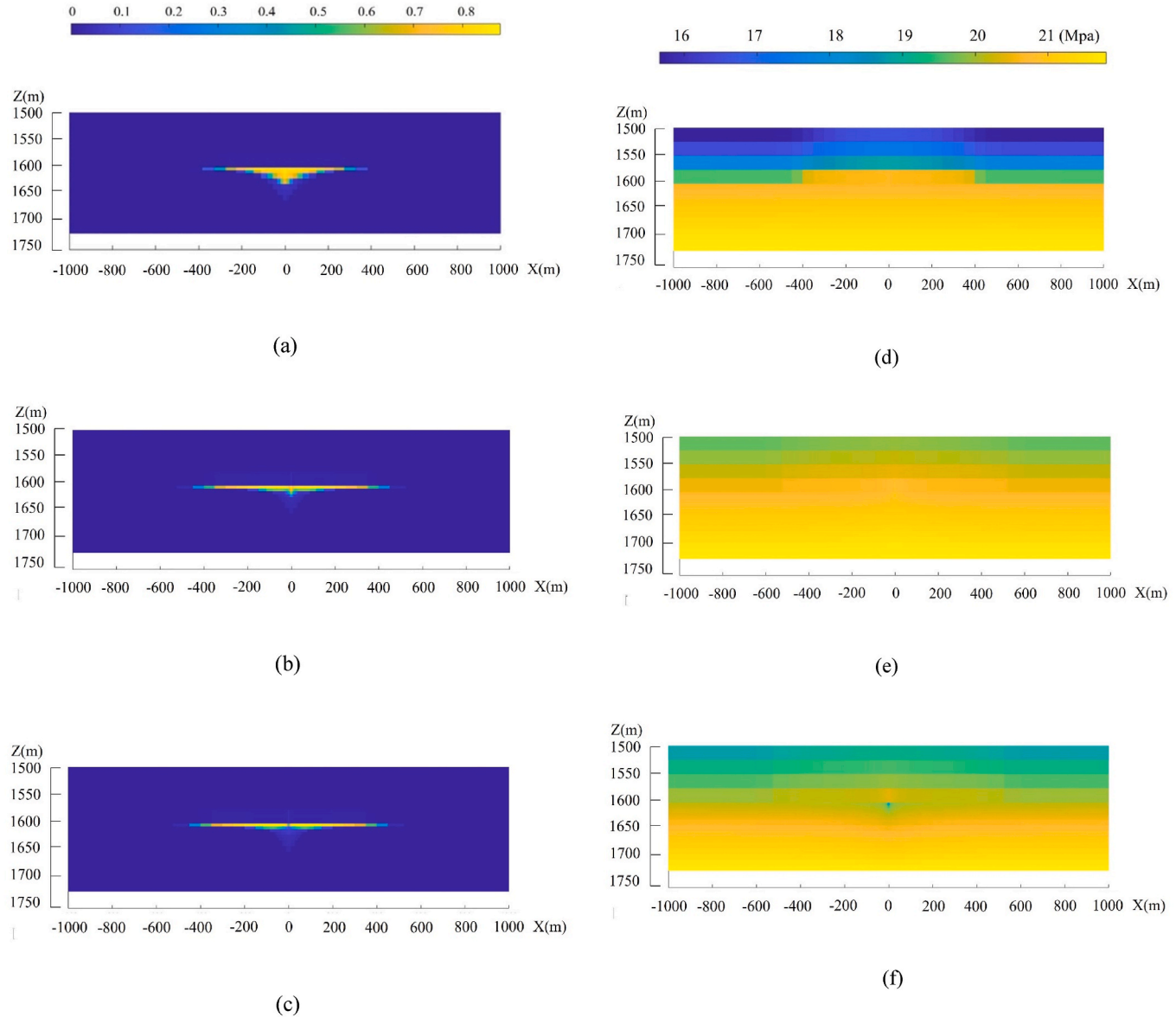

Fig. 5. Numerical results of base model for air saturation profile: (a) after injection of cushion gas; (b) after the last injection; and (c) after the last production cycle. Simulated pore pressure distribution profile (d) after injection of cushion gas, (e) after the last injection and (f) after the last production cycle. (All profiles are at the cross section of Y = 0 m).

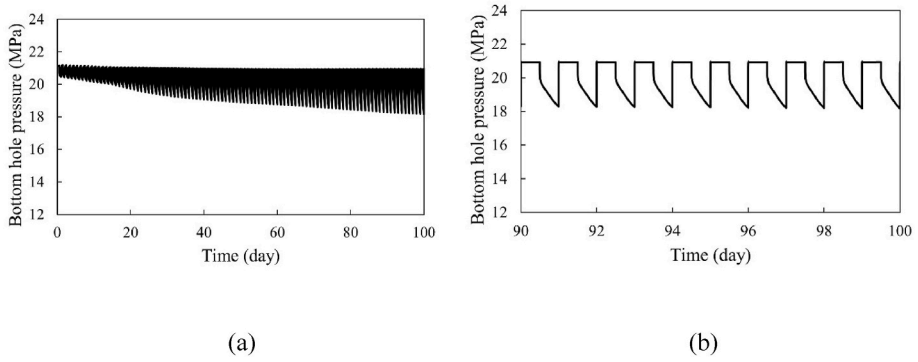

Fig. 6. Numerical results of well bottom hole pressure from the base model in (a) 0–100 cycles, and (b) 90–100 cycles.

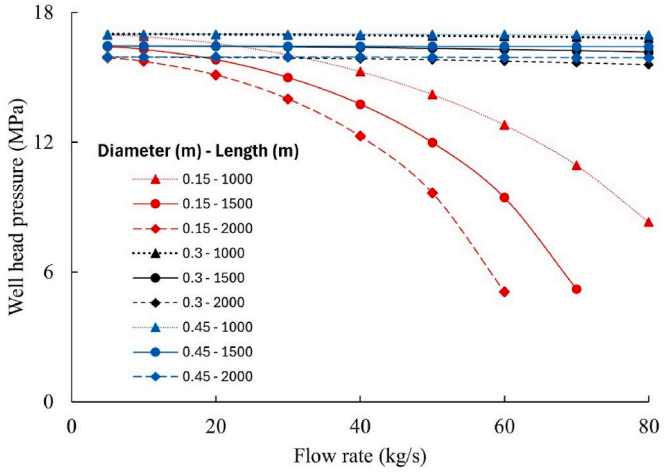

Fig. 7. Well head pressure in production well with different diameter and length versus flow rate for bottom hole pressure of 18.2 MPa.

with the size of most existing gas wells. Then the injection and production well head pressures for the base model were 20.0 MPa and 16.4 MPa respectively. On the other hand, the temperature loss within the well was relatively reduced compared with the cases with well diameter of 0.15 m. As shown in Fig. 8(a), the temperature losses within the well for the base model are 3 K and 2 K for injection and production respectively.

3.3. Near-isothermal process and entire cycle performance

With the available well head pressures and temperatures for both injection and production phases, the energy and round-trip efficiency could be determined with the thermodynamic analysis of the near-isothermal surface plants. Taking the base model as an example (Fig. 8(a)), the inlet pressure and temperature for the expander were 18.1 MPa and 346 K (which equals the reservoir temperature), respectively. Assuming the ambient air with the pressure of 0.1 MPa and the temperature of 293 K, the output power was calculated to be 20.5 MW based on Eq. (7). Furthermore, the outlet temperature was 283.6 K from Eq. (8). The temperature was satisfactory as it is slightly higher than the dew point of 283 K, which shows that the near-isothermal system can be successfully applied for the base model without the need of fuel combustion for air reheating. By using Eqs. (7) and (8) for the compressor, the input power was calculated as 24.0 MW, then the round-trip efficiency for the entire daily cycle for the base model was 61.9 %, as obtained from Eq. (9). All key results of an entire daily cycle from the base model are summarised in Fig. 8 (a). A sensitivity analysis was conducted to illustrate how the selected parameters impact the I-CAES performance in terms of output power and round-trip efficiency. A total of 256 cases were simulated using MRST, and the detail of all values of the four parameters are shown in Table 2. The losses in the well and surface plants, the input and output powers and the round-trip efficiency for all 256 cases were calculated accordingly. The results of the sensitivity analysis indicated the best scenario to be the reservoir with the aquifer depth, thickness, permeability and porosity of 2100 m, 100 m, 5000 mD and 0.1, respectively. The impact of each geological parameter on I-CAES performance was measured by sensitivity index (SI), which is shown in Table 3. It can be seen that the output power is dominated by the aquifer depth, while both permeability and depth are major factors influencing the round-trip efficiency. The details of all relevant values within a whole cycle for the base model and the favourite model are reported in Fig. 8(b), and the round-trip efficiency was 67.3 %, which is much higher than that of two existing D-CAES sites (42 % and 54 % respectively) (Hounslow et al., 1998; Stys, 1983).

4. Uncertainty analysis: A case study of Gippsland Basin

The numerical results are then used for the storage potential assessment of the entire studied region under geological uncertainties.

Table 2
Parameters from Gippsland basin and values chosen for reservoir modelling, where the values in bold are for the base model.

Parameters	Range from Gippsland Basin	Chosen values for sensitivity study in reservoir modelling
Permeability	100–5000 mD	100 mD, **1000 mD**, 3000 mD, 5000 mD
Porosity	10 %–30 %	10 %, **17 %**, 23 %, 30 %
Depth of top aquifer	500–2000 m	600 m, 1100 m, **1600 m**, 2100 m
Thickness of aquifer	100–2500 m	**100 m**, 900 m, 1700 m, 2500 m

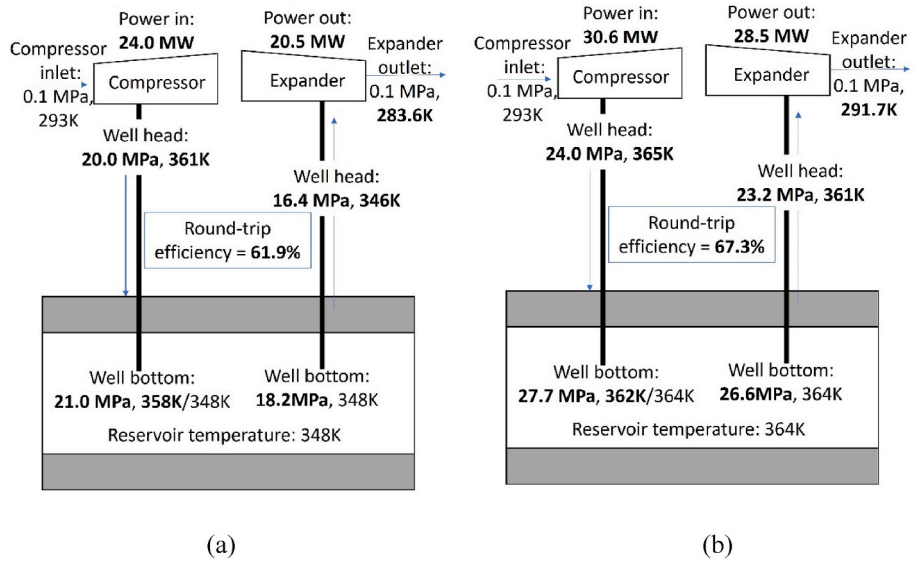

Fig. 8. Summary of numerical results of the: (a) base; and (b) favourable scenarios. (Note: the non-bold and bold data indicate inputs and calculated results, respectively).

Table 3
Sensitivity index (SI) for output power and round-trip efficiency from the sensitivity study.

	Permeability	Porosity	Depth	Thickness
Output power	0.19	0.03	0.69	0.09
RTE	0.37	0.12	0.38	0.13

In this section, the machine learning models are first trained as the proxy model to replace simulation. Geostatistical analysis is then performed to estimate the geological parameters for the whole studied area. Finally, an uncertainty analysis using Monte Carlo approach is used for estimating the overall storage potential.

4.1. Acquisition of predictive machine learning model

Since it is time consuming to conduct the reservoir performance analysis using MRST for a new case with input parameters different from those in Table 2, predictive machine-learning models were developed next to establish the relations between the output power, round-trip efficiency and all relevant parameters within the I-CAES model for reducing the computational cost. Four reservoir parameters (porosity, permeability, aquifer depth and thickness) are identified as critical predictors in the ML models. Results from 256 cases in sensitivity analysis were used for training the ML models, where 30 % data points were used for training while 70 % were used for validation. The regression trends of ML models for both output power and round-trip efficiency are shown in Fig. 9. With the R^2 values of 0.97 and 0.91 respectively, the ML models can provide enough accuracy to predict the output power and round–trip efficiency in the range of all the parameters shown in Table 2.

4.2. Geological analysis: Spatial distribution of all parameters

The uncertainty analysis requires the regional permeability, porosity, depth and thickness maps for each zone with a single I-CAES system as an input for estimating the energy storage potential. The core data from 32 existing gas/oil fields are extracted for developing the full maps of all four reservoir parameters with a spatial interpolation using the Kriging method. The spatial distributions of four parameters within the Central Deep area in Gippsland Basin estimated by the ordinary Kriging method are shown in Fig. 10. The MAE and the R^2 values for all four parameters are smaller than 1 % and larger than 0.96 respectively, which indicates a high level of predictive accuracy.

4.3. Uncertainty analysis: Estimation of overall storage potential and efficiency

The overall performance of the I-CAES system in the Central Deep area was assessed using a Monte Carlo approach. The values of all four reservoir parameters for each grid were obtained from the geostatistical analysis. The Monte Carlo sampling was then applied to represent each parameter as a distribution. With the Monte Carlo analysis, the uncertainty within the reservoir can be quantified, including the variance of depth (which results in potential variance of initial pressure distribution) and thickness.

Besides of the mean values, the cumulative probability of 95 % and 90 % was also used to present the results of uncertainty analysis for each single CAES grids. For example, the value with a cumulative probability of 90 % means that 90 % of the results are above this threshold. The results from the uncertainty analysis coupled with ML model for the distribution of output power across the Central Deep area are shown in Fig. 11, in which Fig. 11(a)and(b) represent the threshold values with a cumulative probability of 95 % and 90 %, respectively, and (c) shows the mean value. The value of the output power ranges significantly, with its mean value varying from 0 to 40 MW, with the highest power found at the southeastern region. Comparing with Fig. 10, this region overlaps with the deepest aquifers. Also, high output power with over 30 MW is observed within the middle south region where the aquifer has a high permeability, around 5000 mD. The results indicate that the aquifer depth is the most crucial parameter which positively dominates the output power, while permeability also entails an important contribution. Similarly, Fig. 11(d)–(f) show the distribution of round-trip efficiency for the values with 95 % and 90 % cumulative probability and the mean value. The mean efficiency ranges from 34.7 % to 67.3 % with over 58 % area having the efficiency over 50 %. Higher efficiency values were observed within the middle south, southern-east and middle north regions. Permeability was the most significant parameter for the round-trip efficiency, as the middle south area has the highest efficiency where the reservoir has the most pervious aquifers. The northwestern region has the lowest output power due to shallower aquifer depth and smaller permeability, while lowest RTE is observed at the region around X = 50 m, Y = 75 m due to extremely low permeability as well as shallow depth and thicker layers. Based on the results, the region with high permeability and deeper aquifer is optimal for site selection. Smaller thickness within the range of this study is also beneficial for increasing the round-trip efficiency.

Based on the results of power distribution, the overall storage potential of the study area for a daily cycle with 12h injection and 12h

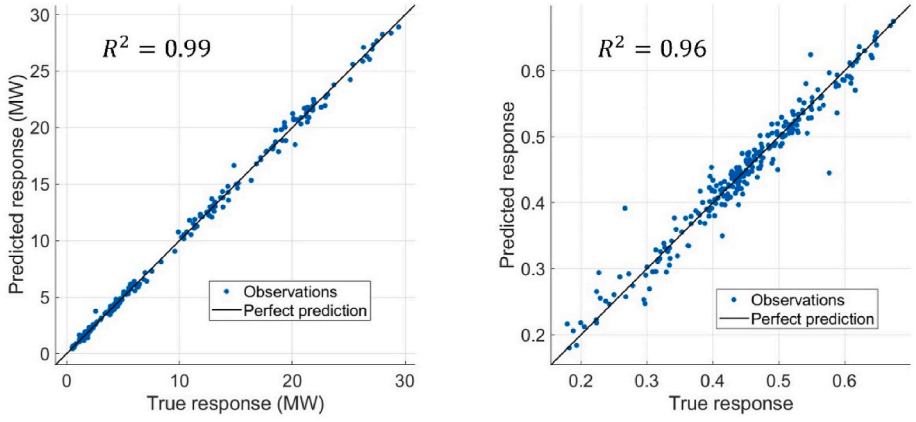

Fig. 9. Results from machine learning being trained by numerical results for: (a) output power; and (b) round-trip efficiency.

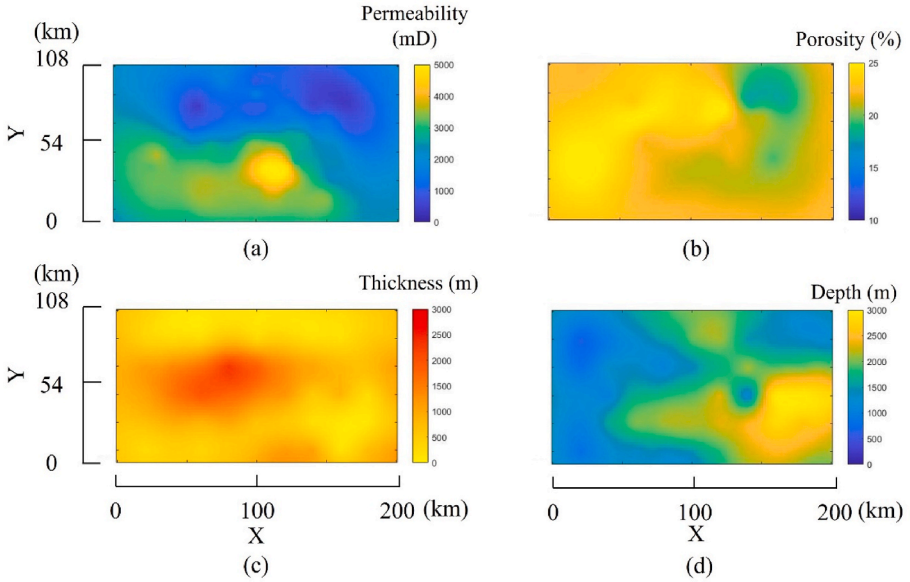

Fig. 10. Distribution of: (a) permeability; (b) porosity; (c) thickness; and (d) depth predicted through the geostatistical analysis using the ordinary Kriging method.

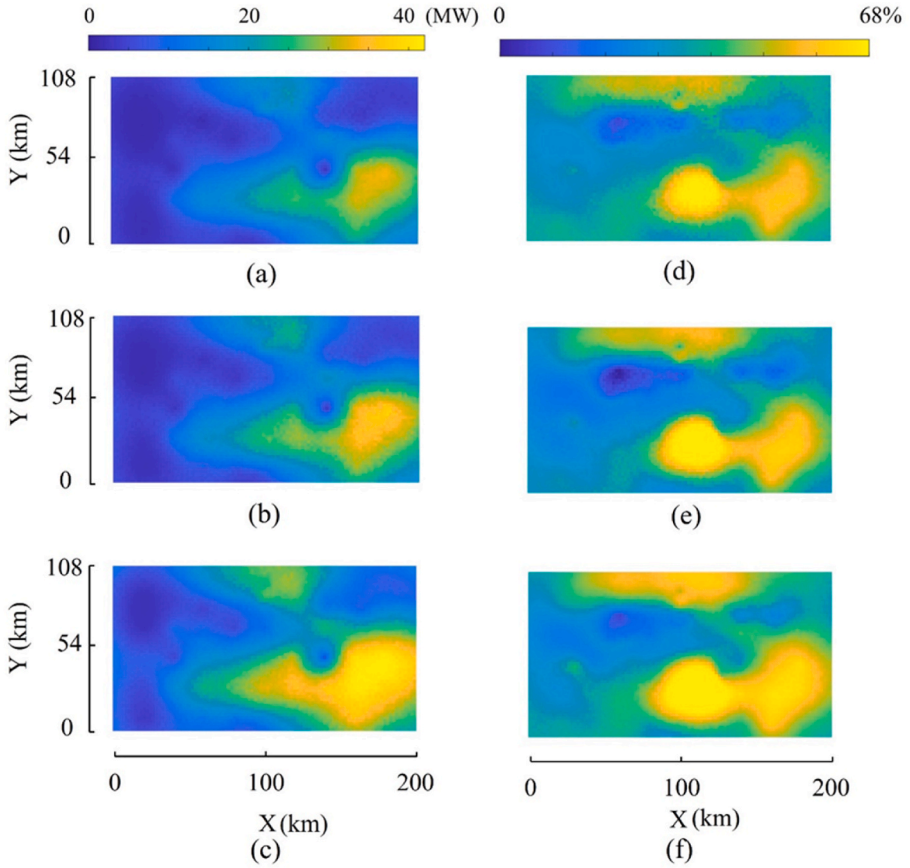

Fig. 11. Output power and round-trip efficiency map for the near-isothermal CAES in the Central Deep area with various confidence levels based on Monte Carlo analysis. Output power map with: (a) 95 % cumulative probability; (b) 90 % cumulative probability; and (c) mean value. Round-trip efficiency map with: (d) 95 % cumulative probability; (e) 90 % cumulative probability; and (f) mean value.

production versus the cumulative probability is calculated and summarised in Fig. 12. It is worth noting that the probability in Fig. 12 represents the probability of the total storage potential being larger than the corresponding value. For example, the storage potential at 90 % probability is 0.88 TWh. The potential energy storage ranges from 0.88 TWh (90 % cumulative probability) to 1.48 TWh (10 % probability) with a mean value of 1.18 TWh. Furthermore, the mean energy storage filtered by the round-trip efficiency is shown in Fig. 13. The overall storage potential of the sites with above any values of RTE can be visualised. For example, the mean overall storage potential for the RTE

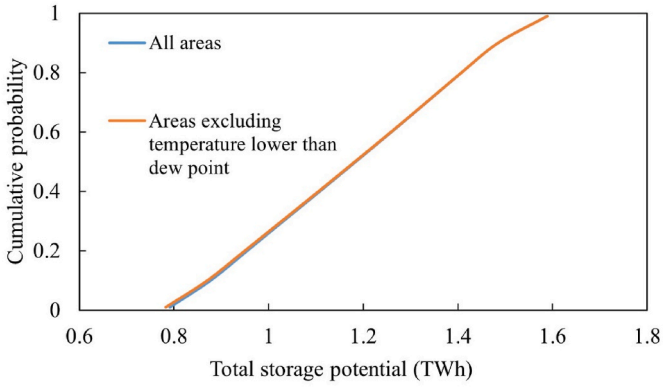

Fig. 12. Cumulative probability of exceeding the total storage potential in the Central Deep area.

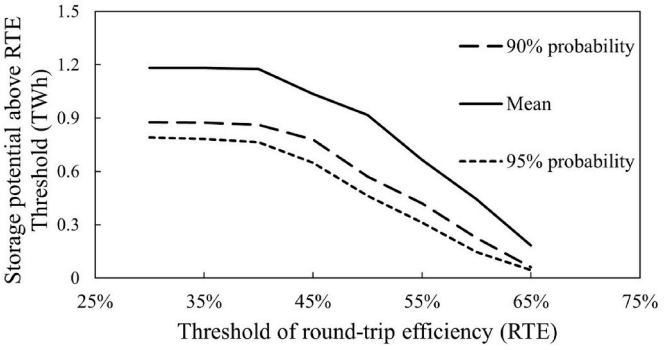

Fig. 13. Summary of total storage potential with round-trip efficiency. The storage capacity here is the sum of the storage potential of the areas with the RTE exceeding corresponding threshold (For example, the mean capacity is 0.917 TWh at RTE = 50 %, which means that a total storge capacity of 0.917 TWh could be achieved from all the sites with RTE over 50 %).

of 50 % is about 0.97 TWh, which means that the sites with the RTE being over 50 % can provide an energy storage of 0.97 TWh. About 0.9 TWh can be provided by the area with the efficiency over 50 %, which indicates that most of the studied area is feasible for the proposed air storage. The lines representing the threshold of a cumulative probability of 95 % and 90 % are also represented in Fig. 13. The overall trends are similar with the potential storage dropping significantly at an RTE of approximately 45 %–50 %. The sites with an RTE over 50 % can still provide over 50 % of the energy storage regarding the overall potential. With Fig. 13, the overall storage potential of sites with any threshold of RTE can be obtained, and the mean storage as well as the values with 90 % and 95 % probability are included. The results from the uncertainty analysis proves the feasibility of the proposed I-CAES in the studied area regarding not only the significant overall storage ability but also the high RTE for over half of the available sites.

4.4. Results of cost estimates

Based on the equations from Section 2.5, the LCOE of the base model is calculated as 0.11 US$/kWh. The capital cost of the compressor and the expander makes a major contribution to the LCOE, while the effect of well cost and O&M cost is relatively modest. In addition, there are over 400 existing gas/oil production wells throughout the Central Deep area of Gippsland Basin (Malek, 1998), and over 90 % of them are potentially satisfactory for being reused at minimum retrofitting costs. Furthermore, the LCOE of all I-CAES grids within the studied area is calculated using the mean value of all the geological parameters. As shown in Fig. 14, the calculated LCOE within the region ranges from 0.04 US

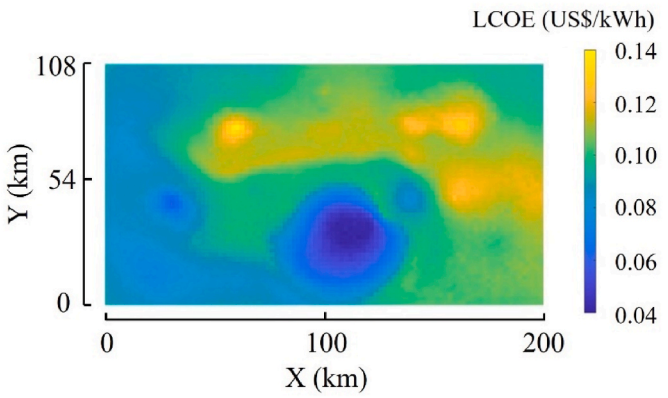

Fig. 14. LCOE map for the near-isothermal CAES in the Central Deep area.

$/kWh to 0.14 US$/kWh.

5. Discussions and conclusions

In this study, an integrated method was developed to assess the performance of near-isothermal CAES system in aquifers. The study showed the significant capacity and promising features of the near-isothermal CAES in aquifers for utility-scale energy storage. Widely distributed aquifers provide significant underground storage for compressed air without occupying land surface. The storage potential of 1.18 TWh was estimated for Gippsland Basin alone, which is more than two times of the existing pumped hydro storage (0.553 TWh) and about 47 times of largest battery storage in Australia (2.4 GWh). Moreover, while the production duration of these energy storage systems is up to hours (*e.g.*, up to 4 h and 12 h for battery and pumped hydro systems respectively), CAES is capable of providing daily cycles and potentially weekly or even seasonal cycles for storage options.

Regarding the technology of CAES, results also showed that the I-CAES to be more advantageous than the traditional D-CAES. By the modelling of a single I-CAES system, it was found that aquifers with proper geological conditions are feasible for developing CAES. The highest round-trip efficiency could reach 67.3 %, which is higher than that of the traditional D-CAES systems around 50 % (Guo et al., 2021; Hounslow et al., 1998). The temperature of the output air for most areas in the Gippsland Basin would be higher than the dew point, which indicates that there is almost no need to reheat air with fuel combustion. Additionally, this also leads to a higher round-trip efficiency. Among all the parameters for underground reservoir, permeability and aquifer depth were identified as the most crucial ones to impact the performance of I-CAES, while the former parameter is more dominant for the output power and the latter has more impact on the round-trip efficiency. The loss of round-trip efficiency is mostly originated from the pressure loss in reservoir and the efficiency within surface plants, while the pressure and temperature reduce within the injection/production wells is minor when the well is properly designed (*e.g.*, by increasing the well radius) and thermally insulated. As for the surface plants, the mechanical efficiency of the compressor and expander highly influences the round-trip efficiency. Also, the selection and design of heat transfer enhancement machinery can have an important role in achieving a near-isothermal process. The temperature of output air will be possibly under the dew point with insufficient heat transfer enhancements.

Based on the economic assessment of this study, the LCOE of the proposed I-CAES is 0.04–0.14 US$/kWh, which is more cost-effective comparing to pumped hydro energy storage systems (~0.15–0.25 US $/kWh) and batteries (~0.15–0.30 US$/kWh) (Al Zohbi, 2022; Xu et al., 2022). Beside of the lower LCOE than other energy storage systems, the proposed I-CAES can effectively reduce green-house gas emission by excluding the usage of combustors, which can meet the Australia's Net

Zero target of achieving net zero green-house gas emissions by 2050 as well as a short-term target of reducing emissions by 43 % below 2005 levels by 2030 (Parliament of Australia, 2022). Moreover, renewable energy especially wind energy is becoming the main source of electricity generation (AEMO, 2025), and CAES will be significant to reduce wind energy curtailment. The co-location of the large-scale I-CAES with wind farms will play a crucial role in balancing the differences between energy supply and demand.

It is found that the machine learning model is capable of predicting the power and round-trip efficiency after trained by sufficient numerical results, which significantly reduced the computational cost for uncertainty analysis. The results from Monte Carlo analysis indicate that the geological uncertainty have significant impact on the overall performance. In summary, this study demonstrates the enormous potential of the proposed I-CAES systems to be adopted in aquifers under a wide range of geological conditions. The proposed system can be operated for cycle duration of 12 h, which is longer than batteries. The estimated overall storage potential within the studied area is over 1 TWh, which is capable of supporting a city with population of 5 million. Wide distribution of pervious aquifers worldwide also allows its strong promise of deployment. I-CAES is cost-effective in the consideration of its relatively low LCOE, minimisation of surface land usage as well as exclusion of combustors. The simulation and uncertainty in this study are based on I-CAES grids of 2 km by 2 km with fixed flow rate. Future research could be conducted to further investigate the impact of scalability in terms of system design on the I-CAES performance. This could be achieved by a multi-objective optimization study of the overall performance. Future study could also consider chemical reactions and other types of CAES systems such as A-CAES.

CRediT authorship contribution statement

Zifeng Cheng: Writing – original draft, Visualization, Validation, Software, Methodology, Formal analysis, Data curation, Conceptualization. **Daniel Dias-da-Costa:** Writing – review & editing, Visualization, Supervision, Methodology, Investigation, Funding acquisition, Formal analysis, Conceptualization. **Yixiang Gan:** Writing – review & editing, Visualization, Supervision, Methodology, Conceptualization. **Sheng Jiang:** Writing – review & editing, Visualization, Methodology, Conceptualization. **Luming Shen:** Writing – review & editing, Visualization, Supervision, Project administration, Methodology, Investigation, Funding acquisition, Formal analysis, Conceptualization.

Declaration of competing interest

The authors declare that they have no known competing financial interests or personal relationships that could have appeared to influence the work reported in this paper.

Acknowledgments

This work was supported in part by the Australian Research Council through Discovery Projects Scheme (DP200101919 and DP230100749). The authors acknowledge the use of the National Computational Infrastructure (NCI) which is supported by the Australian Government, and accessed through the Sydney Informatics Hub HPC Allocation Scheme, which is supported by the Deputy Vice-Chancellor (Research), University of Sydney.

Data availability

Data will be made available on request.

References

AEMO, 2024. Electricity Price and Demand Visualization. Melbourne, Australia. https://aemo.com.au/aemo/apps/visualisations/elec-nem-priceanddemand.html. (Accessed 1 August 2024).
AEMO, 2025. National electricity Market (nem). Melbourne, Australia. https://aemo.com.au/energy-systems/electricity/national-electricity-market-nem. (Accessed 10 January 2025).
Al Zohbi, G., 2022. Cost models for pumped hydro storage system. Encycl. Energy Storage. Amsterdam, Netherlands 157–163.
Allen, R., Doherty, T., Erikson, R., Wiles, L., 1983. Factors Affecting Storage of Compressed Air in Porous-Rock Reservoirs. Pacific Northwest National Lab. (PNNL), Richland, Washington.
Allen, R., Doherty, T., Kannberg, L., 1985. Summary of Selected Compressed Air Energy Storage Studies. Pacific Northwest National Lab. (PNNL), Richland, Washington.
Bennett, J.A., Fitts, J.P., Clarens, A.F., 2022. Compressed air energy storage capacity of offshore saline aquifers using isothermal cycling. Appl. Energy 325, 119830.
Cengel, Y.A., Boles, M.A., Kanoglu, M., 2020. Thermodynamics: an Engineering Approach, ninth ed. in SI units. McGraw-Hill Education, Singapore.
Cheekatamarla, P.K., Kassaee, S., Abu-Heiba, A., Momen, A.M., 2022. Near isothermal compressed air energy storage system in residential and commercial buildings: techno-economic analysis. Energy 251, 123963.
Corey, A.T., 1954. The interrelation between gas and oil relative permeabilities. Prod. Mon. 19, 38–41.
Department of Climate Change, Energy Environment Water, 2024. Gippsland, Victoria Declared Offshore Wind Area. Canberra, Australia. https://www.dcceew.gov.au/energy/renewable/offshore-wind/areas/gippsland. (Accessed 1 September 2024).
Denholm, P., Mai, T., 2019. Timescales of energy storage needed for reducing renewable energy curtailment. Renew. Energy 130, 388–399.
Dib, G., Haberschill, P., Rullière, R., Revellin, R., 2021. Thermodynamic investigation of quasi-isothermal air compression/expansion for energy storage. Energy Convers. Manag. 235, 114027.
Elio, J., Phelan, P., Villalobos, R., Milcarek, R.J., 2021. A review of energy storage technologies for demand-side management in industrial facilities. J. Clean. Prod. 307, 127322.
Fukai, I., Keister, L., Ganesh, P.R., Cumming, L., Fortin, W., Gupta, N., 2020. Carbon dioxide storage resource assessment of cretaceous- and jurassic-age sandstones in the atlantic offshore region of the northeastern United States. Environ. Geosci. 27 (1), 25–47.
Ghorbani, B., Mehrpooya, M., Ardehali, A., 2020. Energy and exergy analysis of wind farm integrated with compressed air energy storage using multi-stage phase change material. J. Clean. Prod. 259, 120906.
Guo, C., Li, C., Zhang, K., Cai, Z., Ma, T., Maggi, F., Gan, Y., El-Zein, A., Pan, Z., Shen, L., 2021. The promise and challenges of utility-scale compressed air energy storage in aquifers. Appl. Energy 286, 116513.
Hagoort, J., 2005. Prediction of wellbore temperatures in gas production wells. J. Pet. Sci. Eng. 49 (1), 22–36.
Hohn, M.E., 1999. Geostatistics and Petroleum Geology, second ed. Springer, Netherlands, Dordrecht.
Hounslow, D.R., Grindley, W., Loughlin, R.M., Daly, J., 1998. The development of a combustion system for a 110 Mw caes plant. J. Eng. Gas Turbines Power 120 (4), 875–883.
Hurter, S., Marmin, N., Probst, P., Garnett, A., 2013. Probabilistic estimates of injectivity and capacity for large scale Co2 storage in the Gippsland Basin, Victoria, Australia. Energy Proc. 37, 3602–3609.
King, M., Jain, A., Bhakar, R., Mathur, J., Wang, J., 2021. Overview of current compressed air energy storage projects and analysis of the potential underground storage capacity in India and the UK. Renew. Sustain. Energy Rev. 139, 110705.
Kushnir, R., Ullmann, A., Dayan, A., 2010. Compressed air flow within aquifer reservoirs of CAES plants. Transp. Porous Media. 81, 219–240.
Li, R., Tao, R., Yao, E., Chen, H., Zhang, H., Xu, X., Wang, H., 2023. Comprehensive thermo-exploration of a near-isothermal compressed air energy storage system with a pre-compressing process and heat pump discharging. Energy 268, 126609.
Li, Y., Liu, Y., Hu, B., Li, Y., Dong, J., 2020. Numerical investigation of a novel approach to coupling compressed air energy storage in aquifers with geothermal energy. Appl. Energy 279, 115781.
Li, Y., Yu, H., Li, Y., Luo, X., Liu, Y., Zhang, G., Tang, D., Liu, Y., 2023. Full cycle modeling of inter-seasonal compressed air energy storage in aquifers. Energy 263, 125987.
Li, Y., Yu, H., Tang, D., Li, Y., Zhang, G., Liu, Y., 2022. A comparison of compressed carbon dioxide energy storage and compressed air energy storage in aquifers using numerical methods. Renew. Energy 187, 1130–1153.
Lie, K.-A., 2019. An Introduction to Reservoir Simulation Using Matlab/Gnu Octave: User Guide for the Matlab Reservoir Simulation Toolbox (MRST). Cambridge University Press, Cambridge.
Lie, K.-A., Møyner, O., 2021. Advanced Modelling with the Matlab Reservoir Simulation Toolbox (MRST). Cambridge University Press, Cambridge.
Mahmoud, M., Ramadan, M., Olabi, A.-G., Pullen, K., Naher, S., 2020. A review of mechanical energy storage systems combined with wind and solar applications. Energy Convers. Manag. 210, 112670.
Malek, R.M.K., 1998. Oil and Gas Resources of Victoria. Department of Natural Resources and Environment. https://earthresources.efirst.com.au/product.asp?pID=573&cID=6. (Accessed 1 June 2023).
Matos, C.R., Pereira da Silva, P., Carneiro, J.F., 2023. Economic assessment for compressed air energy storage business model alternatives. Appl. Energy 329, 120273.

Mouli-Castillo, J., Wilkinson, M., Mignard, D., McDermott, C., Haszeldine, R.S., Shipton, Z.K., 2019. Inter-seasonal compressed-air energy storage using saline aquifers. Nat. Energy 4 (2), 131–139.
Muskat, M., Meres, M.W., 1936. The flow of heterogeneous fluids through porous media. J. Appl. Phys. 7 (921), 346–363.
O'Brien, G., Tingate, P., Divko, L.G., Harrison, M., Boreham, C., Liu, K., Arian, N., Skladzien, P., 2008. First Order Sealing and Hydrocarbon Migration Processes, Gippsland Basin, Australia: Implications for Co2 Geosequestration.
Oldenburg, C.M., Pan, L., 2013a. Porous media compressed-air energy storage (Pm-caes): theory and simulation of the coupled wellbore–reservoir system. Transport Porous Media 97 (2), 201–221.
Oldenburg, C.M., Pan, L., 2013b. Utilization of CO2 as cushion gas for porous media compressed air energy storage. Greenh. Gases Sci. Technol. 3 (2), 124–135.
Parliament of Australia, 2022. Climate Change Act 2022. Canberra, Australia. https://www.legislation.gov.au/C2022A00037/latest. (Accessed 1 June 2023).
Patil, V.C., Acharya, P., Ro, P.I., 2020. Experimental investigation of water spray injection in liquid piston for near-isothermal compression. Appl. Energy 259, 114182.
Qin, C., Loth, E., 2014. Liquid piston compression efficiency with droplet heat transfer. Appl. Energy 114, 539–550.
Ricciardi, K.L., Pinder, G.F., Belitz, K., 2005. Comparison of the lognormal and beta distribution functions to describe the uncertainty in permeability. J. Hydrol. 313 (3), 248–256.
Schulte, R.H.a.C., Nicholas, Holst, Kent, Huff, Georgianne, 2012. Lessons from Iowa: development of a 270 megawatt compressed air energy storage project in midwest independent system operator. Transm. Distrib. World. Sandia National Laboratories, Nashville, Tennessee.
Stys, Z.S., 1983. Air storage system energy transfer (asset) plants. Proc. IEEE 71 (9), 1079–1085.
Tong, Z., Cheng, Z., Tong, S., 2021. A review on the development of compressed air energy storage in China: technical and economic challenges to commercialization. Renew. Sustain. Energy Rev. 135, 110178.
Varma, S., Michael, K., Ciftci, B., Stalvies, C., 2010. Hydrodynamic assessment of the Gippsland Basin. CSIRO Report EP11235. Perth, Australia. https://publications.csiro.au/publications/publication/PIcsiro:EP11235. (Accessed 1 May 2023).
Vidal-Gilbert, S., Tenthorey, E., Dewhurst, D., Ennis-King, J., Van Ruth, P., Hillis, R., 2010. Geomechanical analysis of the naylor field, Otway basin, Australia: implications for CO2 injection and storage. Int. J. Greenh. Gas Control 4 (5), 827–839.
Wang, B., Bauer, S., 2017. Compressed air energy storage in porous formations; a feasibility and deliverability study. Pet. Geosci. 23 (3), 306–314.
Xu, Y., Pei, J., Cui, L., Liu, P., Ma, T., 2022. The levelized cost of storage of electrochemical energy storage technologies in China. Front. Energy Res. 10, 873800.
Yang, L., Cai, Z., Li, C., He, Q., Ma, Y., Guo, C., 2020. Numerical investigation of cycle performance in compressed air energy storage in aquifers. Appl. Energy 269, 115044.
Yu, H., Engelkemier, S., Gençer, E., 2022. Process improvements and multi-objective optimization of compressed air energy storage (CAES) system. J. Clean. Prod. 335, 130081.
Zhang, X., Xu, Y., Zhou, X., Zhang, Y., Li, W., Zuo, Z., Guo, H., Huang, Y., Chen, H., 2018. A near-isothermal expander for isothermal compressed air energy storage system. Appl. Energy 225, 955–964.
Zhong, H., Wang, Z., Zhang, Y., Suo, S., Hong, Y., Wang, L., Gan, Y., 2024. Gas storage in geological formations: a comparative review on carbon dioxide and hydrogen storage. Mater. Today Sustain. 26, 100720.
Zhou, Q., Du, D., Lu, C., He, Q., Liu, W., 2019. A review of thermal energy storage in compressed air energy storage system. Energy 188, 115993.
Zhou, Q., He, Q., Lu, C., Du, D., 2020. Techno-economic analysis of advanced adiabatic compressed air energy storage system based on life cycle cost. J. Clean. Prod. 265, 121768.
Ziegler, M.S., Mueller, J.M., Pereira, G.D., Song, J., Ferrara, M., Chiang, Y.-M., Trancik, J. E., 2019. Storage requirements and costs of shaping renewable energy toward grid decarbonization. Joule 3 (11), 2867–2869.